J Sol-Gel Sci Technol (2016) 78:339–346
DOI 10.1007/s10971-016-3964-9

ORIGINAL PAPER: SOL-GEL AND HYBRID MATERIALS FOR BIOLOGICAL AND HEALTH (MEDICAL) APPLICATIONS

Synthesis and characterization of calcium oxyboroapatite with bimodal porosity

Anastasia Vassilakopoulou[1] · Konstantinos Dimos[2] · Vasilis Kostas[2] · Michael A. Karakassides[2] · Ioannis Koutselas[1]

Received: 18 October 2015 / Accepted: 13 January 2016 / Published online: 2 February 2016

Abstract Calcium oxyboroapatite with bimodal porosity and proposed general formula $(CaO)_x(PO_{2.5})_y(BO_{1.5})_z$ with $10 \geq x \geq 9$, $y \geq 4$ and $z \geq 1.6$ have been prepared for the first time, by thermal processing of sol–gel-derived glass. F-127 triblock copolymer was incorporated in the sol–gel reactions as the structure directing agent under acidic conditions, whereas tributyl borate, triethyl phosphate and calcium nitrate were used as precursors for the glass structure. The prepared materials were chemically analyzed and characterized by X-ray diffraction (XRD), infrared absorption and Raman scattering spectroscopic techniques, where the related XRD patterns clearly revealed growth of rich in boron oxyboroapatite phase with increasing temperature. The oxyboroapatite phases treated at high temperatures exhibited bioactivity after soaking in simulated body fluid (SBF) solution within a few hours and these were observed by μ-Raman and scanning electron microscopy (SEM). Moreover, the external morphology of these materials has been directly observed with SEM microscopy before and after the immersion in SBF. Furthermore, mercury intrusion porosity measurements were taken in order to investigate the porosity, showing bimodal meso- and macro-porosity.

Graphical Abstract

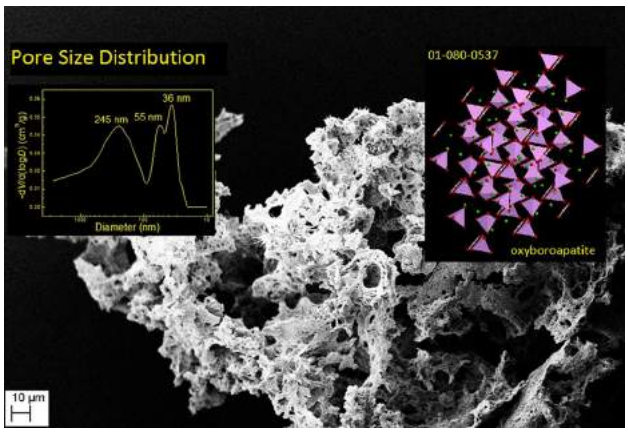

Keywords Sol–gel · Bimodal porosity · Mesoporous · Calcium oxyboroapatite · Bioactive · Glasses

1 Introduction

Apatite materials $M_{10}(PO_4)_6X_2$ where M = Ca or Sr, and X = F, Cl, Br or OH have traditionally been synthesized by various methods involving high temperatures, such as solid-state reactions involving temperatures from 1000 to 1500 °C such as in [1], flux methods, for example, in [2], with temperatures above 1100 °C, fast microwave synthesis as well as with various lower temperature methods. Some of these later are, hydrolysis [3], precipitation, precipitation by double decomposition, wet precipitation [4] and finally sol–gel processes [5]. Hydrothermal treatments [6] can be used for conversion of one type to another as well. Moreover,

✉ Ioannis Koutselas
ikouts@upatras.gr

[1] Materials Science Department, University of Patras, 26504 Patras, Greece

[2] Department of Materials Science and Engineering, University of Ioannina, 45110 Ioannina, Greece

nanocrystalline apatites can be formed with similar methods as read in the reviews in [7]. In all cases, apatite formation and the final material are controlled through a multitude of parameters. Moreover, and in relation to the results of this work, a special case of new apatite phases, in particular oxyboroapatite and hydroxyboroapatite, has been studied by Ternane et al. [8, 9]. The group synthesized nonporous apatite with high-temperature reactions and found the existence domain of pure apatitic oxyborophosphates with the general formula $Ca_x(PO_4)_yB_zO_t$. In these compounds, boron is incorporated as BO_3^{3-} ions in the PO_4^{3-} sites and as linear BO_2^- ions located in channels of crystals. It is worthwhile to mention efforts of the Ternane group to dope these boroapatites with Yb or Eu and to produce application-focused fiber materials [10, 11]. Finally, it has not been reported until now a method to use sol–gel bioactive glasses in order to reach oxyboroapatite materials. The most well-known bioactive silicate glass codenamed 45S5, Bioglass®, has a typical composition of 45 % SiO_2, 24.5 % Na_2O, 24.5 % CaO and 6 % P_2O_5 and has been of primary interest in biological applications [12] being bioactive, due to its SiO_2 concentration, as well as due to the high content of Na_2O and CaO and the large ratio of calcium to phosphorus in the system [13], leading to useful applications [14, 15]. Many techniques have been used to synthesize bioglasses producing various structures including macroporous scaffolds, mesoporous particles and nanofibrous structures [16]. In order to use bioactive glasses, especially the oxyboroapatite systems, it would be ideally required to have similar chemical stoichiometry to that of hydroxyapatite or boroapatite.

Bioactive glasses and specifically borophosphate—not containing silica—glasses, with high CaO/P_2O_5 molar ratio (>1.5) have a high potential for use as biomaterials because their chemical composition is close to that of natural bone [17], and thus, such glasses have been synthesized recently [18]. However, these last reported bioactive glasses have been prepared with melt-quenching techniques, while other such pure calcium borophosphate glasses have not been reported. Boron, besides being catalyst for bioactivity, facilitates the manufacturing process of the phosphate glasses. Boron trioxide (B_2O_3) is regarded as the most capable glass former oxide as the melt does not crystallize even with very small cooling rate. In addition, it provides improvement to the mechanical and chemical properties of phosphate glasses [19] and allows the possibility to change the coordination number of boron from 3 to 4 and vice versa, thus, being susceptible to hydrolysis as well as to the creation of B–OH bonds when exposed to moisture. Such bonds act as catalysts for bioactivity as it has been similarly observed to the active groups: Si–OH, Ti–OH, Zr–OH, Nb–OH and Ta–OH [20].

The present work is devoted to the scope of synthesis and the structural characterization of new porous oxyboroapatite materials using borophosphate sol–gel porous glasses as precursor materials, based on a technique introduced in early 1990s [21]. Also, in parallel, another main objective was to include boron, due to the fact that it had been observed that the reported well-characterized glasses obtained from fast quenching of boron-containing calcium phosphate glasses did have strong bioactive behavior [20]. In addition, strong motive was toward the synthesis of this type of material in porous form with the ability to tune the pore size and the final chemical stoichiometry through the use of sol–gel reaction. In this fashion, it could have been possible to synthesize bioactive borophosphate materials with needed porosity for biological applications, however, using low-temperature synthesis. In order to induce porosity to the final material, a route can be followed where the reaction occurs within the regions of micelles formed in an aqueous or nonaqueous solution. An important nonionic surfactant with uses throughout the scientific field is the triblock polymer F127(PEO–PPO–PEO). The synthesis of this type of induced porosity via the use of F127 can lead to a variety of materials in general. In the cases reported here, as well as others that have not been reported and lie beyond the scope of bioactive porous materials, the usage of ethanol/water/F127 in the particular ratios allows the creation of hydrophobic/hydrophilic micelles that lie in the L1 region (micellar—lyotropic phase liquid crystal) of their relevant phase diagram. In detail, the less hydrophilic components such as tributyl borate and triethyl phosphate probably reside in the region formed by the polypropylene oxide chains, while the calcium ions reside in the region to the polyethylene oxide chains of F127. Therefore, upon drying the final product is being formed by first inducing boron—phosphorus connectivity to which calcium ion diffuses and binds in a secondary process. Thus, it is expected that these materials will have high content in boron.

Finally, the glass materials that were synthesized and characterized were also subjected to heat treatment in order to improve the results analysis and verify to be compatible with oxyboroapatite, a system only reported in the past by Ternane et al. [8, 9].

2 Materials and methods

2.1 Materials

All chemicals were purchased from Sigma-Aldrich. Nonionic block copolymer $EO_{97}PO_{67}EO_{92}$ (F127, Mw = 12,600). As starting materials were used: triethyl phosphate [$(C_2H_5)_3PO_4$, Mw = 182.15, (TEP)], calcium nitrate [$Ca(NO_3)_2 4H_2O$, Mw = 236.16, (CaNt)] and tributyl borate [$(CH_3CH_2CH_2CH_2O)_3B$, Mw = 230.15,

(TBB)]. Hydrochloric acid (HCl) and absolute ethanol (Eth, 99 %). All chemicals were used without further purification.

2.2 Synthesis

Porous ternary phosphoborate glasses were prepared by the standard sol–gel reactions using as starting materials $Ca(NO_3)_2 4H_2O$ (CaNt), $(C_2H_5)_3PO_4$ (TEP) and $(CH_3CH_2CH_2CH_2O)_3B$ (TBB) with defined proportion. The ternary system was synthesized by using a nonionic surfactant, Pluronic F127 as mesostructure directing agent. In a typical synthesis, 1.6 g of F127 was dissolved in 20 mL of absolute ethanol at room temperature with 1 g of a 2-M HCl solution and 3.08 g of H_2O. Afterward, the appropriate amounts of CaNt, TEP and TBB were added under continuous stirring for 1 h. Reactant compositions for the synthesis of samples presented here are shown in Table 1. The samples were heated at 450 °C for 1 h in porcelain crucibles to evaporate nitrates and water. Also, these samples were heated at different temperatures from 450 °C, up to 1050 °C for characterization purposes as well as to develop the evacuation of the pores from organic template and the formation of apatite-like crystalline phases.

2.3 Characterization

X-ray powder diffraction (XRD) on the samples were carried out on a D8 Advance system (Bruker) with Cu ($\lambda = 1.54178$ Å) radiation. The voltage and current applied to the X-ray tube were 40 kV and 40 mA. The graphs were measured in the 2θ range from 2° to 80°. The step rotation was 0.02°, and the scanning speed was maintained at 1 s/step.

Infrared spectra were measured on a Fourier transform spectrometer (Digilab) in the form of powder pressed within anhydrous KBr pellets. The final spectra were the average of 20 scans in the frequency range of 400–4000 cm^{-1}, at 2 cm^{-1} resolution. ATR(Pike) measurements were also taken for the sake of comparison and showed no differences.

Raman spectra were obtained from samples in the form of small pieces with a micro-Raman system using the 532-nm (Nd-YAG) line of a laser diode operating at 60 mW for excitation. Raman scatter was collected by an optical microscope (Leica) equipped with lenses 10×, 50× and 100×. The probing spot was about 2 μm in diameter when using the 100 × lens in the microscope. The spectrometer was calibrated by recording the spectrum from a Si sample with characteristic Raman peak at 520.7 cm^{-1}.

Mercury intrusion porosity measurements were taken with a Quantachrome PoreMaster-33 GT instrument. Pore size distribution was constructed according to the Washburn equation: $D = -(4\gamma\cos\theta)/P$, where D is the pore diameter expressed in μm, γ is the mercury surface tension (480 dyne/cm), θ is the contact angle between mercury and the pore wall (140°), and P is the applied pressure in psi.

The surface morphology of the samples was observed by scanning electron microscopy (SEM) (EVO-MA10, Bruker) using LaB_6 as electron source. The surface chemical analysis was carried out by energy-dispersive X-ray spectroscopy (EDX) analysis using the SEM microscope electron beam, while in many cases the photographs were acquired without gold coating on the sample and in these cases a highly fast data acquisition mode was used in conjunction to low beam current and averaging in order to produce good quality images without significant charging effects.

Additional, the in vitro bioactivity of the produced materials was studied. The SBF solution was prepared with ion concentrations nearly equal to those of the human blood plasma in 500 mL batches and was continuously checked for pH and possible precipitates throughout the period that portions of it were used in the in vitro bioactivity tests of the prepared materials. The samples, c.a. 1.5 mg, were soaked in 7 mL of simulated body fluid (SBF) in polyethylene containers maintained at 37 °C and pH = 7.4. After specific periods of time, the samples were removed and studied by μ-Raman spectroscopy and SEM.

3 Results and discussion

Figure 1 shows the powder XRD patterns of OBA1 and OBA2 after heat treatment at different temperatures as placed on appropriate silicon substrate. Reflection bands of interest were observed in the range of the angles $2\theta = 30°$–36°, while even at temperatures as low as 450 °C the creation of semicrystalline apatitic matrix can be detected both in OBA1 and in OBA2. At 800 °C, OBA1 showed extra reflections between 30° and 32° (Fig. 1c), while OBA2 at 1050 °C exhibits a shoulder at slightly larger than 30.5° (Fig. 1f). The differences are attributed to the varying concentration of the boron units into the hydroxyapatite (HA) structure (Fig. 1i) which affects its XRD pattern.

Table 1 Composition of the materials investigated (**o**xyboroapatite samples 1 and 2)

	F127 (g)	TBB (g)	CaNt (g)	TEP (g)	H_2O (mL)	Eth (mL)	HCl 1 M/2 M (mL)
OBA1	1.6	2.42	4.13	1.61	3.08	20	1
OBA2	3	2.9	1.52	1.61	–	20	0.36

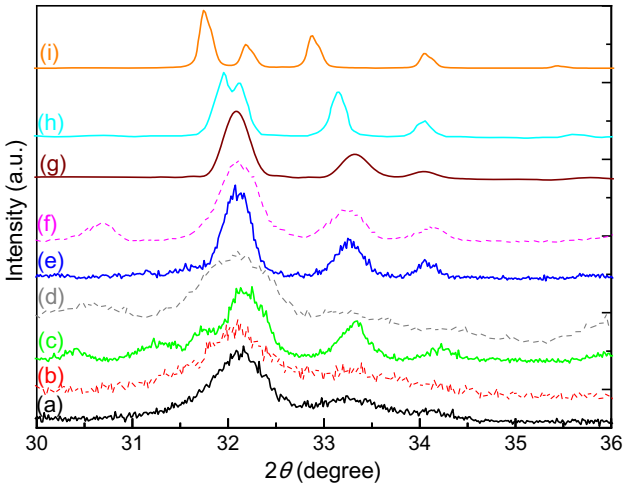

Fig. 1 X-ray diffraction patterns of OBA1 at 450 °C (*a*), OBA2 at 450 °C (*b*), OBA1 at 800 °C (*c*), OBA2 at 800 °C (*d*), OBA1 at 1050 °C (*e*), OBA2 at 1050 °C (*f*), an oxyboroapatite phase with a 12.64 % boron content (adapted from ref. 8) (*g*), an oxyboroapatite phase with a 9 % boron content (adapted from ref. 8) (*h*) and hydroxyapatite (*i*)

OBA1 and OBA2 have been synthesized with different types of micelles, where no water was used in OBA2. Therefore, the integration of the boron units in the structure is initiated by different concentration in the formed precursor micelles. The main difference between the XRD patterns [8, 9] of the OBA1/OBA2 and HA is that the splitting between the two major lines (211) at 31.7° and (112) at 32.2° of HA decreases in boroapatite with increasing boron content and finally convolutes to one band when the content is above 12 % mol, as OBA1 and OBA2 become one peak at 32.15°, as shown in Fig. 1f, e, respectively. Characteristic example of bibliographic XRD patterns of low (9 %) and high (12 %) boron content is shown for comparison purposes as Fig. 1h, g, respectively. Therefore, based on the similarities of the XRD patterns of both OBA1 and OBA2 to the bibliographic data, it is implied that both are typical oxyboroapatite structures with boron content above 12 % and by further comparison with refs [8] and [10], the formula should be suggested to be close to $9.0CaO{\cdot}4.0PO_{2.5}1.9BO_{1.5}$. Also, as discussed further, from EDX analysis at least this phosphorus to boron ratio, i.e., $\sim$2, content can be verified. The differences of the diffraction reflection peaks of OBA2 compared with OBA1 is the appearance of peaks in the spectra of OBA2 (2θ: 32.2°, 37.4°, 53.8°), the latter not shown in Fig. 1, which are assigned to the CaO cocrystallization at temperatures above 1000 °C. The peaks appearing for the samples OBA1 and OBA2 at relatively low temperatures at 30.4, 31.4 and 31.7 as well as the small peak at 30.7 for Fig. 1g pattern are peaks that are due to the impurities and/or metastable phases, disappearing at higher temperatures, not related to the oxyboroapatite phase. In particular, all these peaks can be related to phases of calcium carbonate, calcium borate and boron oxide, with ICDD cards 005-0586, 022-0139 and 01-076-0781, respectively. The interesting observation is that all these peaks disappear at high temperatures.

In these type of materials, most of the vibrational bands, as observed in the IR and Raman spectra, are due to the vibrations of isolated tetrahedral units as PO_4, BO_3 and BO_4 which have different sets of vibrational frequencies, also dependent on the interconnectivity of these units and the ending of chains of units. In this sense, the terminal oxygen of the previously named units which are connected to other units are labeled as Ø (bridging), while the oxygen which are not connected to other units are labeled simple as O. IR spectra of OBA1 and OBA2 are shown in Fig. 2 and are dominated by four major absorption bands centered around 1440, 1250, 1050 and 570 cm^{-1}. The strongest at c.a. 1050 cm^{-1} is assigned to the v_3 antisymmetric stretching modes of PO_4^{3-}, while the one at c.a. 570 cm^{-1} is due to the v_4 bending modes of PO_4^{3-}. On the other hand, boron addition has its the main effect in the IR spectra the development of the absorption band at 1440 cm^{-1} which can be solely attributed to the presence of $B\emptyset_2O^-$ groups as well as the band centered at 1250 cm^{-1} due to the triangular boron BO_3^{3-} units. Further, carbonate units, such as in calcite and aragonite, absorb in the same region, around 1400 cm^{-1} with parallel absorption at 870 cm^{-1}. On the other hand, boron oxide exhibits absorption bands between 1200 and 1300 cm^{-1} (asymmetric stretch of trigonal borate units) and 720 cm^{-1} (bending modes) show bending modes of the bridged units B-O-B. These phases were detected in the relevant XRD patterns and using that basis we can also ascribe the IR peaks to the vibrations of the XRD detected phases. In

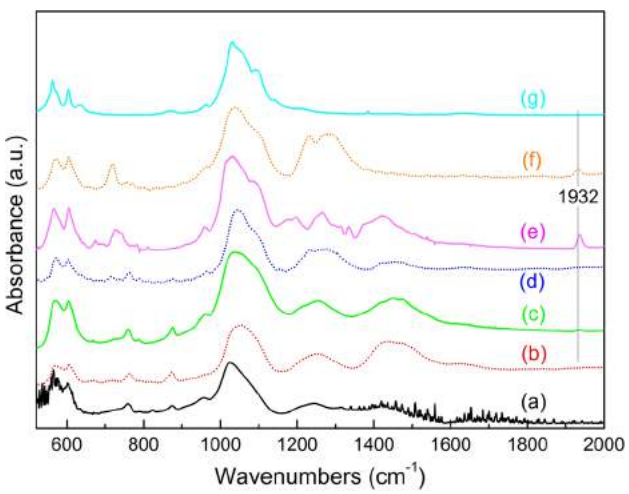

Fig. 2 Infrared absorbance spectra of OBA1 at 450 °C (*a*), OBA2 at 450 °C (*b*), OBA1 at 800 °C (*c*), OBA2 at 800 °C (*d*), OBA1 at 1050 °C (*e*), OBA2 at 1050 °C (*f*) and hydroxyapatite (*g*)

addition, the peak at 762 cm^{-1} belongs probably to bending modes of boron tetrahedra in calcium borate phases, also detected in the XRD patterns which are being considered impurities to the oxyboroapatite structure. In fact, all the phases giving rise to the previously small IR peaks vanish at high temperatures, as their XRD patterns do vanish, with the exception of the 720-cm^{-1} peak which is due to the borate units. It is very important to emphasize that the weak peak at 1932 cm^{-1} is attributed to the antisymmetric stretching mode of B-O bonds of linear borate groups, BO_2^- [8]. This unit is a part of the oxyboroapatite unit, while the other minor peaks are considered metastable impurities. According to the same authors, boron is twofold coordinated in these glasses as BO_2^- in the channels of the apatitic structure and as triangular BO_3^{3-} groups substituting PO_4 as well as OH groups, which explain our observations concerning the characteristic IR absorption peaks by boron units. Moreover, it appears that OBA1 is more amorphous than OBA2 as deduced by the comparison of their respective spectra. It may well be assumed that OBA2 is a mixture of glass–ceramic boroapatite and borate glass.

Figure 3 shows the Raman spectra of OBA1 at 800 and 1050 °C, after soaking in SBF solution and that of HA. The spectra of OBA2 and OBA1 are almost identical, and thus, OBA2 spectra are not shown for simplicity. In the OBA1 spectrum at 1050 °C (Fig. 3b), similar to that treated at 800 °C, the strongest line situated at 960 cm^{-1} is attributed to the v_1 symmetric stretching mode of PO_3^{4-} ions, while the weak peak at 1049 cm^{-1} has been assigned to the v_3 antisymmetric stretching mode of PO_4. Also, the peaks at 586 and 430 cm^{-1} can be attributed to the v_4 antisymmetric bending (out of plane) and the v_2 symmetric bending modes of PO_4 groups, respectively. The peaks at 910 cm^{-1} and at 930 cm^{-1} are probably due to the different interconnected types of BO_3^{3-} groups which coexist with the previous phosphate ones because of the high proportion of boron in the samples. According to Ternane et al., the peak at 910 cm^{-1} is symmetric stretch of BO_3^{3-} [8, 9]. The remaining peaks correspond to degenerate situations arising due to the thermally induced crystalline field.

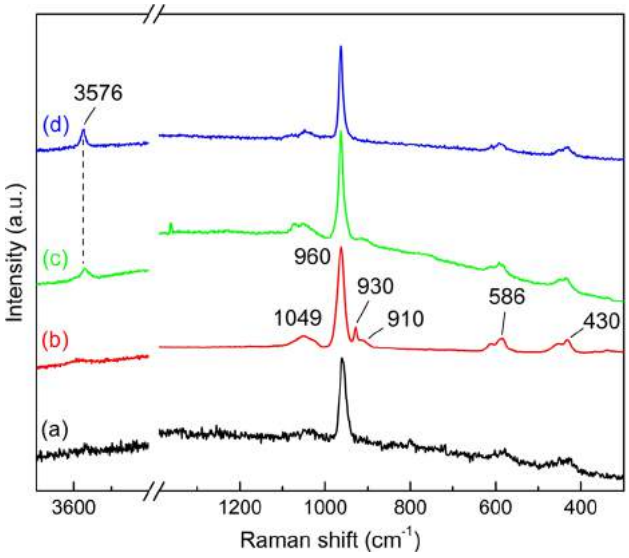

Fig. 3 Raman spectra of OBA1 at 800 °C (*a*), OBA1 at 1050 °C (*b*), OBA1 at 1050 °C after soaking in SBF solution (*c*), and hydroxyapatite (*d*)

Figure 3 shows also a typical Raman spectrum of the samples before and after soaking in SBF solution. The main difference that was observed, after soaking in SBF solution for 50 days (Fig. 3c) in relation to the sample before soaking in SBF (Fig. 3b), is the observation of the peak 3576 cm^{-1} which is characteristic of HA formation. In addition, peaks due to the borate units are being diminished due again to the HA formation and the spectrum resembles that of HA. In some spectra corresponding to short SBF immersion times, the poor crystallinity of the newly formed surface layer yielded broad and low-intensity peaks for the characteristic HA bands.

Mercury intrusion porosimetry was employed to reveal the porous character of the materials. A typical pore size distribution curve for OBA2 heated at 800 °C is shown in Fig. 4. As observed, the material exhibits a wide pore size distribution with pore diameters from 20 nm up to above 2 μm. Nevertheless, three maxima are present at 36, 55 and 245 nm. These results come in full agreement with SEM observations taking also into account that due to the pore filling mechanism, mercury porosimetry will always slightly underestimate pore sizes compared to SEM observations [22]. In addition, fundamental porous characteristics of the sample were determined. Total pore volume was calculated at 0.60 cm^3/g, while its specific surface area was estimated to be 13 m^2/g.

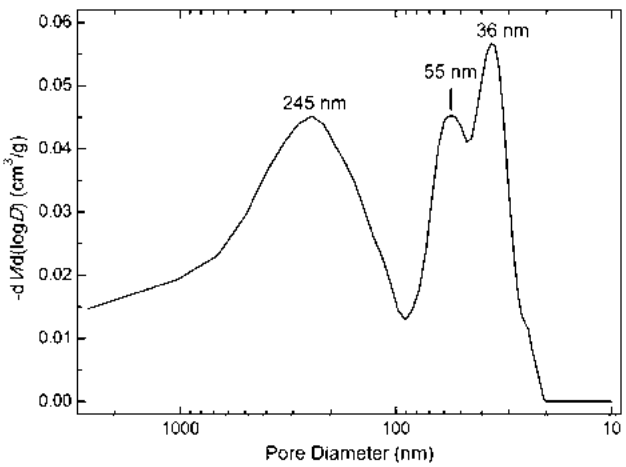

Fig. 4 Pore size distribution obtained by mercury intrusion porosimetry for OBA2 (800 °C)

Finally, and complementary to the abovementioned techniques, energy-dispersive X-ray spectroscopy (EDX) analysis confirms the existence of boron in both OBA1 and OBA2 samples, which were thermally treated at 1050 °C, where boron content appears as a low intensity but totally discrete peak, while phosphorus and calcium are also detected as well (Fig. 5). The carbon peak is due to the carbon wafer being observed below the sample. The low-intensity appearance of the boron peak in Fig. 5 (left) can be compared to the signal of a reference compound such as BPO_4, concluding that the boron content is that the ratio of P/B is at least 2. Full stoichiometric analysis has been carried out;, however, due to the porosity of the samples, the least chemical composition that can be safely deduced is that the boron content is at least 12 %mol, as described further below.

In order to study the bioactivity and the ability of calcification of the system, all samples, treated either in high or in low temperatures, were soaked in SBF solution and EDX measurements and SEM observations were made after 1, 7 and 50 days. In addition, glass slides were used as reference sample for checking if the SBF solution produced precipitation materials onto various surfaces by itself. From Fig. 6(left), it is obvious that there is no hydroxyapatite on the surface of the reference sample since the double P peak at c.a. 2 keV as well as the Ca peaks is missing. In contrast, HA growth on OBA1 sample after soaking in SBF solution is confirmed by EDX analysis (Fig. 6 right).

Heat-treated at 1050 °C, OBA1 and OBA2 samples were immersed in SBF and exhibited rapid deposition of HA on the surface even after 5 h of immersion as seen in SEM images (Fig. 7). The top row images of Fig. 7 show the deposition after just 5 h of immersion, while on the middle row of Fig. 7, which corresponds to 50 days of immersion, particles that have been created with an average diameter of 100 nm are being observed covering the porous surface of the samples. For comparison reasons, the SEM images of OBA1 at 450 and 800 °C before immersion in SBF are shown in Figs. 7e, f where the porous character of the glass is exposed and no precipitates are observed.

Also, we observe as an example in Fig. 8 that the OBA1 after being immersed in SBF for 50 days shows the formation of hydroxyapatite on its surface as seen with the measured XRD pattern that resembles that of hydroxyapatite but also shows as smaller peaks the peaks of oxyboroapatite phase below the formed hydroxyapatite.

4 Summary and conclusions

In this study, porous oxyboroapatite materials, with proposed stoichiometry and boron content larger than 12 %mol, i.e., proposed formula $9.0CaO{\cdot}4.0PO_{2.5}1.9BO_{1.5}$, have been prepared by means of sol–gel glasses. The synthetic route for the glass preparation involved the use of nonionic

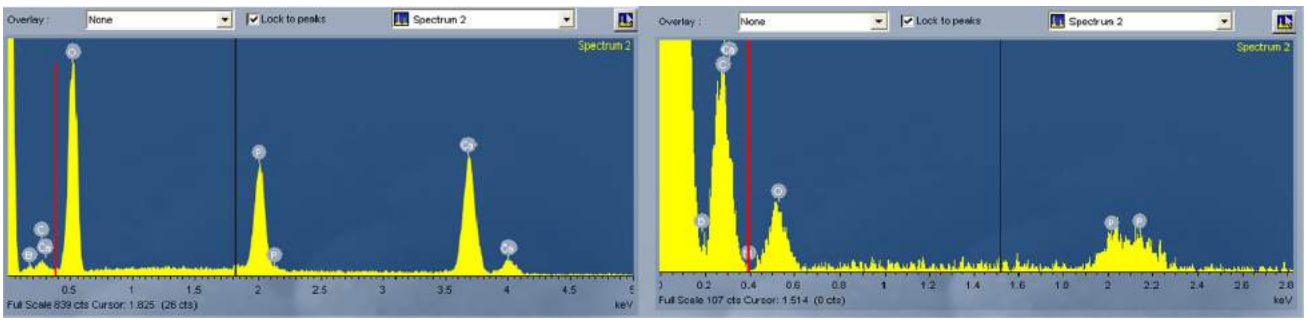

Fig. 5 EDX spectra of OBA1 (*left*) and OBA2 (*right*) both treated at 1050 °C (*red vertical index line* shows the N line)

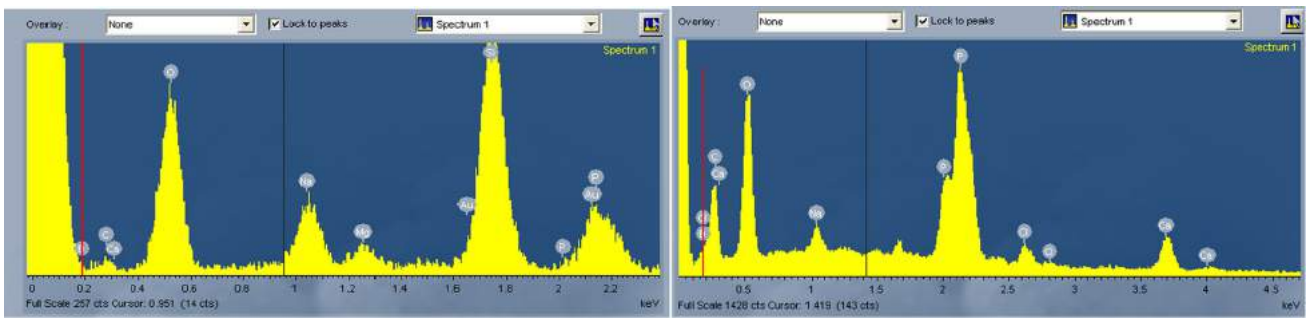

Fig. 6 EDX spectra of reference sample (*left*) and OBA1 (*right*) thermally treated at 1050 °C and after soaking in SBF solution for 50 days

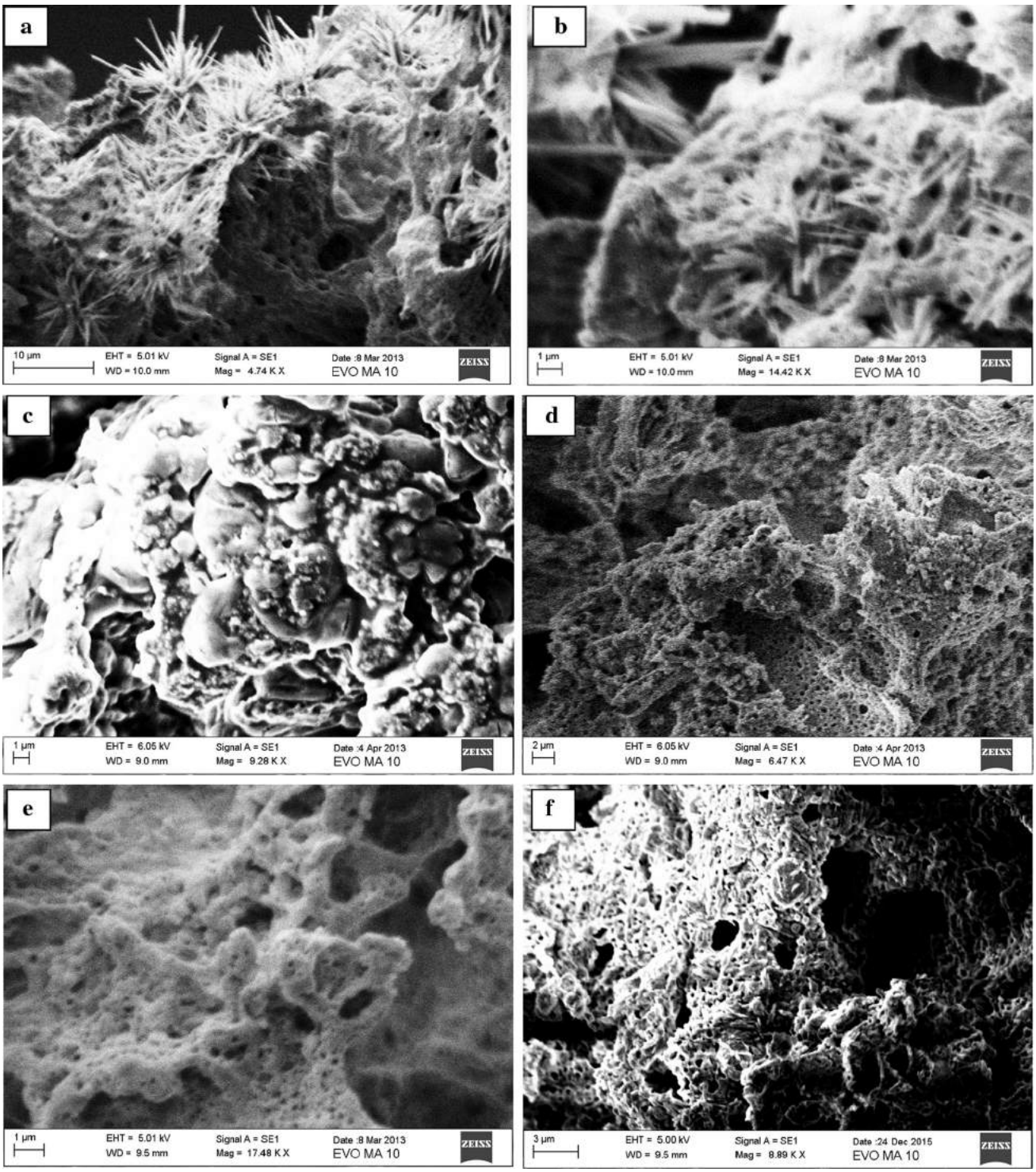

Fig. 7 Representative SEM images of the surface of mesoporous oxyboroapatite glasses (1050 °C) after immersion in SBF solution: **a** OBA1 after 5 h, **b** OBA2 after 5 h, **c** OBA1 after 50 days and **d** OBA2 after 50 days in SBF, **e** OBA1 before SBF immersion and **f** OBA2 before SBF immersion

surfactants to induce porosity and organic precursors that provided boron and phosphorus. Thermal treatment above 800 °C yielded the oxyboroapatite phases with boron content higher than 12 %. Moreover, it is the only instance of such materials being synthesized where bimodal porosity at the macro- and mesoporous scales is observed; property

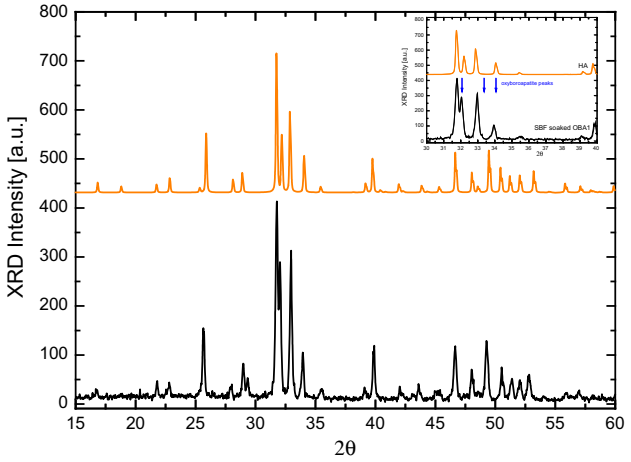

Fig. 8 Representative XRD patterns of hydroxyapatite (*orange*) and that of sample OBA1 (*black*) after being soaked in SBF for 50 days. *Inset* shows the same patterns in the region for 2θ between 30 and 40°, where some of the oxyboroapatite *peaks* are shown in *blue arrows*

that can be affected by the virtue of the surfactant and the timing scale of the synthetic route. Studies are being reported regarding their structure and properties using techniques as XRD, IR, Raman, SEM/EDX as well as their bioactivity by immersion in SBF solution. The initial glass structure that creates the mesoporous matrix appears to be closely related to oxyboroapatite, as observed after heat treatment, by XRD, IR and Raman spectra, which are in agreement with similar results from the literature. These oxyboroapatite materials show immediate bioactivity after soaking in SBF solution within few hours, as verified by the formation of hydroxyapatite phase at their surface, detected by Raman spectra, SEM images and EDX analysis.

Compliance with ethical standards

Conflict of interest The authors declare that they have no conflict of interest.

References

1. Sato M, Kono Y, Ueda H, Uematsu K, Toda K (1996) Bulk and grain boundary ionic conduction in lithium rare earth-silicates "$LiLnSiO_4$" (Ln = La, Nd, Sm, Eu, Gd, Dy). Solid State Ionics 83:249
2. Takahashi M, Uematsu K, Ye ZG, Sato M (1998) Single-crystal growth and structure determination of a new oxide apatite, $NaLa_9(GeO_4)_6O_2$. J Solid State Chem 139:304
3. Monma H, Ueda S, Kanazawa T (1981) Properties of Hydroxyapatite Prepared by the hydrolysis of tricalcium phosphate. J Chem Tech Biotechnol 31:15–24
4. Ramesh S, Natasha AN, Tan CY, Bang LT, Niakan A, Purbolaksono J, Chandran H, Ching CY, Ramesh S, Teng WD (2015) Characteristics and properties of hydroxyapatite derived by sol-gel and wet chemical precipitation methods. Ceram Int 41:10434–10441
5. Montazeriana M et al (2015) Sol-gel synthesis, structure, sintering and properties of bioactive and inert nano-apatite–zirconia glass–ceramics. Ceram Int 41:11024–11045
6. Jingbing L, Xiaoyue Y, Hao W, Mankang Z, Bo W, Hui Y (2003) Preparation of hydroxyapatite nanoparticles by using high-gravity reactive precipitation combined with hydrothermal method. Ceram Int 29:629–633
7. Eichert D et al (2009) Nanocrystalline apatite-based biomaterials. Nova Science Publishers, New York
8. Ternane R, Cohen-Adad MTh, Boulon G, Florian P, Massiot D, Trabelsi-Ayedi M, Kbir-Ariguib N (2003) Synthesis and characterization of new oxyboroapatite. Investigation of the ternary system $CaO–P_2O_5–B_2O_3$. Solid State Ionics 160:183–195
9. Ternane R, Cohen-Adad MTh, Panczer G, Goutaudier C, Kbir-Ariguib N, Trabelsi-Ayedi M, Florian P, Massiot D (2002) Introduction of boron in hydroxyapatite: synthesis and structural characterization. J Alloy Compd 333:62–71
10. Ternane R, Boulon G, Guyot Y, Cohen-Adad MT, Trabelsi-Ayedi M, Kbir-Ariguib N (2003) Crystal growth, structural and spectroscopic characterization of undoped and Yb^{3+} -doped oxyboroapatite fibers. Opt Mater 22:117–128
11. Ternane R, Cohen-Adad MTh, Panczer G, Goutaudier C (2002) Structural and luminescent properties of new Ce^{3+} doped calcium borophosphate with apatite structure. Solid State Sci 4:53–59
12. Hench LL, Paschall HA (1973) Direct chemical bond of bioactive glass-ceramic materials to bone and muscle. J. Biomedical Materials 7:25–42
13. Hench LL (2001) Bioglass and similar materials. In: Encyclopedia of materials: science and technology, 2nd edn. Elsevier, pp 563–568
14. Hench LL (1991) Bioceramics: from concept to clinic. J Am Ceram Soc 74:1487–1510
15. Kokubo T (1991) Bioactive glass ceramics: properties and applications. Biomaterials 12:155–163
16. Yan X, Huang X, Yu C, Deng H, Wang Y, Zhang Z, Qiao S, Lu G, Zhao D (2006) The in-vitro bioactivity of mesoporous bioactive glasses. Biomaterials 18:3396–3403
17. Fabian P, Schwarz K, Epple M (2000) The structure of bone studied with synchrotron X-ray diffraction, X-ray absorption spectroscopy and thermal analysis. Thermochima Acta 361:131
18. Saranti A, Koutselas I, Karakassides MA (2006) Bioactive glasses in the system $CaO–B_2O_3–P_2O_5$: preparation structural study and in vitro evaluation. J Non-Cryst Solids 352:390–398
19. Frieser RG (1975) A review of solder glasses. Electrocomponent Sci Technol 2:163
20. Kokubo T, Kim HM, Kawashita M (2003) Novel bioactive materials with different mechanical properties. Biomaterials 13:2161
21. Hench LL, West JK (1990) The sol-gel process. Chem Rev 90:33–72
22. Garcia I, Azcune I, Casuso P, Carrasco PM, Grande H-J, Cabanero G, Katsigiannopoulos D, Grana E, Dimos K, Karakassides MA, Odriozola I, Avgeropoulos A (2015) Carbon nanotubes/chitin nanowhiskers aerogel achieved by quaternization-induced gelation. J Appl Polym Sci 132: 42547 (1–9)